Journal of Materials Chemistry B

ROYAL SOCIETY OF CHEMISTRY

PAPER

View Article Online
View Journal | View Issue

Cite this: J. Mater. Chem. B, 2025, 13, 2737

Design, development and performance of a Fe–Mn–Si–Cu alloy for bioabsorbable medical implants

J. N. Lemke, *[ab] J. Fiocchi,[b] C. A. Biffi,[b] A. Tuissi,[b] F. Copes,[c] C. Paternoster,[c] D. Mantovani [c] and A. Coda[ab]

Received 25th July 2024,
Accepted 18th December 2024

DOI: 10.1039/d4tb01635a

rsc.li/materials-b

Bioabsorbable metallic alloys constitute a very challenging and innovative field, mainly aimed to develop the next generation of temporary medical implants. Degradation data, biological *in vitro* and *in vivo* tests are of major importance in particular for complex alloys, in which the individual element additions could enhance material performance and add functionalities. In this study, a novel Fe–Mn–Si–Cu alloy was carefully designed for vascular and blood-contact applications, and its microstructure, mechanical behavior, degradation behavior and biological performances were investigated accordingly. In previous studies, Mn and Si were found to be suitable elements to effectively enhance mechanical properties and accelerate corrosion rate in simulated body fluid. Cu was added for further grain refinement by the formation of small Cu-rich particles, potentially impacting mechanical properties and degradation behavior. In addition, the feasibility of inducing antibacterial effects in a Fe–Mn–Si–Cu alloy with low Cu content was investigated. The alloy was prepared firstly on a small scale by vacuum arc remelting, then on a larger scale by vacuum induction melting and converted into sheets by conventional thermomechanical processing techniques. Heat treatments were explored to find optimal microstructure conditions. The results confirm promising mechanical, degradation and biological performance in testing the material in *in vitro* conditions, showing that the degradation products are neither systematically cytotoxic nor have any hemotoxic effects. On the other hand, the expected antibacterial effects could not be confirmed.

1. Introduction

Bioabsorbable alloys for medical implant applications are at the forefront of the biomaterials research attracting high interest by academia and medical industry as they have the potential to enable new elective therapies in cardiovascular and orthopaedic surgery making secondary interventions obsolete, improving patient well-being and reducing stress on the health system. Secondary surgeries for implant removal that become mandatory for children and necessary for adults in case of long-term inflammation or displacement over time, are a severe concern for patients, physicians and the medical system as they are often difficult to perform, causing pain and excessive costs. A novel approach to avoid such surgeries is to replace today's permanent medical implants with temporary ones, which perform their function as long as necessary and are subsequently absorbed by the body. Since the working conditions, biological environment and requirements for the implant vary a lot depending on the implantation side, it is expected that there will be a need for various materials that differ in mechanical and degradation characteristics.[1] As for today, under investigation and limited application in cardiovascular[2] and orthopaedic[3] surgery are polymers, Mg-alloys, Fe-alloys and Zn-alloys.[4] Fe-alloys prevail over the other solutions whenever tuneable degradation times in combination with high mechanical performance are required.[5] The Fe system offers many alloying possibilities for the development of bioabsorbable temporary implants. However, the selection of alloying elements that are biologically compatible or at least tolerable in the human body environment at relevant quantities is limited.[6]

While the slow degradation and the superior mechanical properties of Fe and its alloys pose opportunities for the development of bioabsorbable scaffolds and implants, many experts consider the slow corrosion rate of Fe and Fe-based alloys a fundamental issue that needs to be solved and look out for strategies to accelerate it.[7] Various approaches were

[a] SAES Getters S.p. A., Viale Italia 77, 20045 Lainate (MI), Italy. E-mail: jannisnicolaslemke@cnr.it
[b] CNR ICMATE, National Research Council, Institute of Condensed Matter Chemistry and Technologies for Energy, Via Previati 1/E, 23900 Lecco, Italy
[c] Laboratory for Biomaterials and Bioengineering (LBB), Canada Research Chair Tier I for the Innovation in Surgery, Department of Mining, Metallurgy, and Materials Engineering & Regenerative Medicine, CHU de Quebec Research Center, Laval University, Quebec City G1V 0A6, Canada

investigated to increase the dissolution of Fe-based materials by tailoring material configuration, microstructure and chemistry.

Regarding the design, the realization of porous structures could enhance the degradation by augmenting the surface to volume ratio, exposing more area that can be contemporary dissolved.[8] In addition, porous designs could also allow for fine-tuning the implants elastic modulus, adjusting it to the surrounding tissue, preventing stress shielding.[9] Another recent design approach for enhancing the degradation rate is to cover the metal implant surface with an absorbable polylactide (PLA) coating, which permits the diffusion of electrolytes through the polymeric layer.[10] In this design, the local acidification caused by the dissolution of the PLA prevents the formation of a passivation layer, which would significantly slow the degradation down, allowing to keep a high rate due to the polymer permeability. Based on such a metal–polymer composite material, a biodegradable thin stent of 70 μm strut thickness was developed which also exhibited promising *in vivo* performance when implanted in rats.[11] However, the scalability of this approach was not studied yet as well as the effectiveness of the coating for thicker devices. Ideally, a Fe-based alloy which intrinsically dissolves homogenously and faster than the current available alloy solutions would be an asset.

On this account, a lot of research was and is dedicated to alloying or modifying the composition of existing Fe-based alloys with the scope to increase the degradation rate of the material inherently and many alloys have been proposed in the recent years.[12] Particular attention gained Fe–Mn alloys, as Mn additions to Fe demonstrated to have several beneficial effects, like improved mechanical properties, faster corrosion and reduced magnetic susceptibility.[13] However, literature reports also on controversy about the use of high Mn contents in bioabsorbable materials: while some studies dispute the risk of increased daily dietary intakes,[14] the role of Mn in the blood can be associated with severe neurotoxicity and the daily uptake in of an adult should not exceed 11 mg per day.[15]

Starting from these promising characteristics of the Fe–Mn system, several elements were added to further enhance the structural and functional performance. Among these, Fe–Mn–C[16–18] and Fe–Mn–Si[19–21] are examples for more deeply investigated alloys. Regarding the mechanical properties, but also degradation rate and preliminary biological tests, Fe–Mn–Si showed several encouraging features, leading to the development of quaternary alloys like Fe–Mn–Si–Pd[22] and Fe–Mn–Si–Ca.[23] Especially with the aim to prepare Fe–Mn alloys with antibacterial properties, Ag addition to Fe–Mn were studied.[24–26] Recently, also Fe–Mn–C–Ag alloys were proposed for stenting applications, but while cytotoxicity and hemocompatibility were not adversely affected, the presence of secondary Ag-phases resulted detrimental for the ductility and could be harmful for the fatigue life of the final device.[26]

A similar approach to award antibacterial properties consists in the addition of Cu to Fe–Mn alloys. A Fe–Mn–C–Cu was developed and characterized in artificial urine environment by Ma *et al.*, demonstrating that the synergic effect of degradation and release of Cu ions inhibited the formations of a biofilm.[27] At the same time, they observed a strong antibacterial effect against *S. aureus*. Furthermore, Fe–Mn–C alloys with added Cu were reported to degrade faster either in electrochemical or static corrosion conditions due to the Cu additions, presumably caused by electrogalvanic coupling effect.[28] Paul *et al.* prepared a Fe–30Mn–1C alloy by induction melting and characterized its biological performance with and without 3.5 wt% Cu addition.[29] Both alloys showed an elevated antibacterial performance, but the alloy with Cu addition exhibited an enhanced antibacterial activity against the very aggressive, wild-type bacteria *P. aeruginosa*.

These works suggest that Cu could be a favorable alloying element for Fe–Mn alloys, enhancing biological and degradation performances. However, further testing in adequate *in vitro* and *in vivo* set-ups is necessary to confirm the promising preliminary results that were obtained so far.

In this study, a Fe–Mn–Si–Cu alloy has been prepared by conventional melting, then was thermomechanical processed, and characterized with the aim to obtain suitable mechanical and degradation behaviors for bioabsorbable implant application. The Cu content of 2 wt% was selected considering biological and mechanical aspects, as well as taking into account the recent literature. The scope was to add a low content in order to avoid additional biological concerns, excessive impact on microstructure and the formation of secondary phases that could deteriorate the mechanical properties. Instead, the Cu content should be just enough to provide an anti-bacterial effect. Final heat treatments were explored to favorably impact the materials microstructure and performance, as a function of the envisaged application. Microstructure analysis, mechanical property assessment and degradation testing in potentiodynamic, and static immersion set-ups were conducted. As for the biological performances of the developed alloy, *in vitro* indirect cytotoxicity test towards multiple cell lines, together with hemocompatibility and antibacterial tests were performed. Literature reports ambiguous results on Fe–Mn materials that have been alloyed with Cu and were investigated by cell viability and antibacterial tests. This is partially caused by the small-scale laboratory material preparation and experimental set-ups used in such studies, making an evaluation of the biological performance on an industrial scale unreliable. The aim of this work is to assess for the first time the present bioabsorbable Fe–Mn–Si–Cu alloy, produced by a scalable industrial process, to evaluate the functionality and feasibility of the alloying approach for the preparation of medical devices. Benefits and concerns of this approach are discussed considering the scientific relevance and the limits of the presented *in vitro* test results. The composition of the alloy has been disclosed in a patent, hold by SAES Getters S.p.A.[30,31]

2. Experimental

2.1 Materials and sample preparation

The alloy was prepared from pure element feedstock (Fe and Mn from Faci Europe S.p.A, Si from Metalpolveri S.r.l., Cu from Carlo Erba S.r.l.) by vacuum arc melting (VAR) of bottom

Table 1 Composition of Fe–Mn–Si–Cu alloys, experimental results are the average of 3 measures

	Composition (wt%)			
Alloy	Fe	Mn	Si	Cu
Nominal	66	27	5	2
Experimental (EDX)	66.1 ± 0.3	27.1 ± 0.3	4.7± 0.1	2.2 ± 0.1

shaped ingots with a weight around 60 g. In a second campaign of melting for biological characterization, the alloy was melted using the same pure element feedstock by vacuum induction melting (VIM, using a Balzers VSG10 Furnace) in larger quantities as quadratic ingot of 2.2 kg (length and width = 70 mm). VIM was performed under Ar atmosphere and in an alumina refractory crucible. The nominal alloy formulation and the verification of chemistry by SEM-EDX are shown in Table 1. The chemical composition was determined as average from three different microprobe spots of the sample. A higher accuracy could be achieved by using technique like ICP or XRF, however the control of chemistry should be sufficient for the scopes of this study.

Ingots were homogenized in a muffle furnace and then converted from 70 mm into 2.1 mm – thick sheets by hot rolling (1100 °C) and then to 1.5 mm by cold rolling with final cold work of 25%. Alloy compositions and manufacturing route were designed based on promising results achieved in an earlier work on a ternary Fe–30Mn–5Si alloy,[32] replacing Mn by Cu. This alloy, which was characterized as homogenized ingot and after a final annealing treatment at 600 °C for 1 h will be used as reference in this article.

Pictures of the Fe–Mn–Si–Cu ingot and sheets are shown in Fig. 1.

The alloy was investigated after homogenization of ingot or, in case of cold rolled sheet samples, after a final heat treatment. Specimen for testing were cut by electro-erosion machining (EDM) from both homogenized ingot and rolled sheet in four different configurations:

1. Disc shape for microstructure analysis and corrosion test (d = 16 mm; t_{ingot} = 10 mm/t_{sheet} = 1.5 mm).

2. Dog bone shape for tensile test (w = 7 mm; l = 15 mm; t = 1.5 mm).

3. Rectangular samples for static degradation test (w = 15 mm; l = 15 mm; t = 1.5 mm).

4. Disc shape for biological test (d = 11.3 mm).

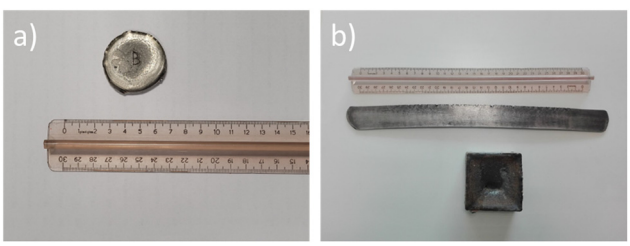

Fig. 1 Ingots and cold rolled sheets: (a) VAR melted button; (b) VIM melted ingot and cold rolled sheet.

Samples for microstructural characterisation were mounted in epoxy resin, prepared by standard metallurgical cutting and grinding procedures using SiC papers up to polishing with 1 μm diamond suspension surface finish, then treated with a Nital-2% etching reagent. Disc samples for electrochemical corrosion test and rectangular sample for static degradation test were polished up to a 1200 mesh smoothness.

2.2 Heat treatments

All heat treatments were performed in a muffle furnace. Homogenization treatment on ingots was performed at 1000 °C for 2 h under flowing Ar atmosphere. Annealing treatments on rolled sheets were conducted in air at three different temperatures for 1 h: 600 °C, 800 °C and 1000 °C. The samples were cooled down by either slow furnace cooling (below 10 °C min^{-1}) or by quenching in water, reaching room temperature in a few seconds.

Heat treatments were performed to prepare the material for four different stages with various scopes:

- Stage I: pre-screening heat treatment study to identify suitable phase composition conditions by X-ray diffraction measurements.
- Stage II: characterization of microstructure and precipitation behaviour by optical microscopy (OM) and scanning electron microscopy (SEM).
- Stage III: mechanical properties characterization by tensile test.
- Stage IV: characterization of corrosion behaviour, degradation behaviour and *in vitro* biological assessment.

A comparison of the effect of all heat treatment conditions on the material microstructure and performance goes beyond the scope of this study. On the contrary, obsolete heat treatments that would lead to expected inferior or not suitable positive outcome for Fe–Mn–Si–Cu as bioabsorbable alloy were sorted out and not further performed in later stages. With this approach, heat treatments at 600 °C for 1 h and 800 °C for 1 h followed by furnace cooling were selected for the characterization of mechanical properties and the later one as the best condition for the complete assessment. In addition, a heat treatment at 900 °C for 1 h was applied only for the characterization of Cu-rich particles precipitation behaviour, to better study their dissolution and formation. An overview on the used heat treatments is shown in Table 2.

2.3 Microstructural analysis

Phases were identified by X-ray diffraction (XRD), using $Cu_{K\alpha}$ (λ = 1.5418 Å) radiation on a θ:θ vertical scan Panalytical X'Pert PRO diffractometer, equipped with parallel (Soller) slits – 0.04 rad – and a real time multiple strip detector, in the 30°–100° 2θ range. Microstructure analysis was performed for the visual identification of microstructural features and grain size determination with an optical microscope (Leitz Aristomet) and a scanning electron microscope (Leo, mod. Leo 1413, operating at 20 kV), equipped with an energy dispersive spectroscopy (EDS) probe.

Table 2 Overview of heat treatments

Condition	Temperature [°C]	Time [hours]	Cooling	Stage
HT600-FC	600	1	Furnace [<10 °C min^{-1}]	I–III
HT800-FC	800	1	Furnace [<10 °C min^{-1}]	I–IV
HT1000-FC	1000	1	Furnace [<10 °C min^{-1}]	I–II
HT600-WQ	600	1	Water quenched	I–II
HT800-WQ	800	1	Water quenched	I–II
HT900-WQ	900	1	Water quenched	II
HT1000-WQ	1000	1	Water quenched	I–II

2.4 Mechanical properties

Mechanical properties were studied at ambient temperature using an MTS 2/M machine equipped with an extensometer, testing dog-bone specimens in tensile configuration according to ASTM E8/E8M with a strain rate of 0.015 min^{-1}. A minimum of 3 samples for each condition was studied.

2.5 Degradation testing

Static immersion tests were performed in an incubator following ASTM G31, while pseudo-dynamic electrochemical tests were conducted with a potentiostat according to ASTM G5-94 R99.

The static immersion test protocol consisted in sterilizing samples by immersion for 5 min in 70 vol% ethanol in deionized water solution. The samples were subsequently fully immersed in modified Hanks' solution (Carlo Erba reagents, composition: 0.14 g l^{-1} $CaCl_2$, 0.10 g l^{-1} $MgCl_2{\cdot}6H_2O$, 0.10 g l^{-1} $MgSO_4{\cdot}7H_2O$, 0.40 g l^{-1} KCl, 0.06 g l^{-1} KH_2PO_4, 0.35 g l^{-1} $NaHCO_3$, 8.0 g l^{-1} NaCl, 0.048 g l^{-1} Na_2HPO_4) for 14 days at 37 °C in an atmosphere containing 5% CO_2 and 85% relative humidity. After extraction, loosely attached corrosion products were removed with ethanol using an ultrasonication bath for 15 min and dried with warm air. Corrosion products, as well as the degraded surfaces of samples, were characterised by microscopy to investigate on the local chemical composition.

Degradation rate (DR) was calculated considering the weight loss according to eqn (1):

$$\mathrm{DR} = \frac{8.76 \times 10^4 W}{A t \rho} \quad (1)$$

where W is the mass loss in g, A is the sample surface area (cm^2), t is the exposure time to the solution (h), and ρ is the atomic density of the material (g cm^{-3}).

Potentiodynamic tests were performed with a VMP3 potentiostat from BioLogic connected to a three electrodes corrosion cell, with the sample acting as working electrode, Pt acting as counter electrode, and Ag/AgCl acting as reference electrode. A home-made phosphate buffered saline (PBS) solution was prepared as corrosion medium for Tafel Plot tests (8.74 g l^{-1} NaCl, 0.06 g l^{-1} $NaHCO_3$, 0.06 g l^{-1} Na_2HPO_4). The differences between the PBS and the Hank's solution used in static immersion test may also have an impact on the corrosion rate in the two here used test setups. However, it may be stressed that the aim of the present work is not to compare directly the results of the two tests by using as similar test conditions as possible, but rather to use the same testing conditions that were applied in previous studies.[32] The solution temperature was controlled at 37 °C (body temperature) applying a steady oxygen flow during testing for simulating closer blood conditions. The samples were inserted into a masked holder reducing the exposed area to 1 cm^2. The testing procedure followed a 3.5 h protocol, starting with measuring the open circuit corrosion potential (OCP) for 1 h, subsequently applying five ramps of corrosimetry with 30 min duration each, *i.e.*, increasing the potential for a small ramp to measure the corrosion resistance without perturbing the natural corrosion process. Then, the corrosion potential and current were calculated using a larger potential ramp from the Tafel plots. Finally, the corrosion current was used to calculate the corrosion rate using the following eqn (2):

$$\mathrm{CR} = \frac{i_{\mathrm{Corr}} \times A \times W}{n \times F \times \rho} \quad (2)$$

where i_{corr} is the corrosion density extracted from the Tafel plot (A), A is the exposed area of the sample (cm^2), W is the weighted molecular weight of the alloy (g), n is the weighted valence state of the ion, F is the Faraday constant, and ρ is the atomic density of the alloy (g cm^{-3}).

2.6 Biological testing – cytotoxicity assay

Before cell seeding, all samples were sterilized by UV irradiation. Briefly, each side of the samples underwent two cycles of UV irradiation for 15 minutes. Then, samples were stored in sterile 24 multi-well plates until use. SS316L was used as a reference material. Four cell lines were used to characterize the effects of the proposed alloy on cell viability: Human Dermal Fibroblasts (HDFs); Human Umbilical Vein Endothelial Cells (HUVECs); Human Umbilical Artery Smooth Muscle Cells (HUASMCs) and Human Bone Osteosarcoma Cells (Saos-2). HDFs represent a general human cellular model, HUVECs and HUASMCs are two vascular cell lines used for material assessment for cardiovascular application and Saos-2 are a widely used cellular model for bone. HUVECs and HUASMCs were isolated in compliance with the Canadian Tri-Council Policy Statement: Ethical Conduct for Research Involving Humans and institutional CHU de Quebec – Laval University guidelines. The protocol was approved by the Ethics Committee of the CHU de Quebec Research Centre (CER #S11-03-168). For the other cell lines, both the HDFs (neonatal human dermal fibroblasts, Cell Application Inc.) and Saos-2 (Sao2-2 HTB85, ATCC) were commercial cells.

To evaluate the effects of the proposed alloy on cell viability, an indirect cytotoxicity assay was performed following the ISO

10993-5:2009 procedure. The area of 1 cm^2 of the masked samples were immersed in 660 µl of basal medium supplemented with 1% P/S for 1, 3 and 7 days and incubated at 37 °C in a saturated atmosphere at 5% CO_2. At each time point, medium of three samples has been collected and was subsequently used for the cytotoxicity test. Cytotoxicity tests have been performed using different concentrations of the extracted media: 100%, 10% and 1% dilutions, respectively.

HDFs, HUVECs, HUASMCs and Saos-2 cells were seeded in the well of 96 multi-well plates at a density of 20 000 cells per cm^2 and incubated at 37 °C, 5% CO_2 for 24 hours in 100 µl per well of the respective complete media. The day after, medium was removed and 100 µl of the 100, 10 and 1% extracts dilutions were added to the well containing the cells and incubated for 24 hours. The extracts were then removed and 100 µl of 1% solution of resazurin sodium salt in the respective complete media were added to the cells and incubated for 4 hours at 37 °C and 5% CO_2. After the incubation, the solutions containing the now reduced resorufin product were collected and fluorescence intensity at a 545 nm_{ex}/590 nm_{em} wavelength was measured with a SpectraMax i3x Multi-Mode Plate Reader (Molecular Devices, San Jose, California, USA). Fluorescence intensity is proportional to cell viability.

2.7 Biological testing – hemocompatibility test

Hemocompatibility tests were performed following the ISO 10993-4:2017 procedure. Whole human blood from a healthy donor was collected in citrate-containing blood collection tubes. Each sample was placed in a 15 ml tube and 10 ml of sterile PBS 1× were added in each tube. PBS 1× was used as a negative control and deionized H_2O as positive control. Samples and controls were incubated at 37 °C for 30 minutes. In the meantime, the collected blood was diluted in PBS 1× to a final ratio of 4 : 5 (4 parts of citrated blood and 5 parts of PBS 1×). After incubation, 200 µl of diluted blood were added in each tube and carefully mixed by inverting each tube. After that, samples and controls were incubated at 37 °C for 1 hour. All tubes were carefully mixed by inversion after 30 minutes of incubation. At the end of incubation, the tubes containing the samples and the controls underwent a centrifugation step at 800*g* for 5 minutes. The supernatant was collected and 100 µl aliquots were placed in a 96-well plate. The absorbance (OD) at a wavelength of 540 nm has been recorded. Haemolysis was calculated as follows.

$$\text{Haemolysis} = \frac{OD_{smple} - OD_{CTRL\ Pos}}{OD_{CTRL\ Pos} - OD_{CTRL\ Neg}} \times 100 \qquad (3)$$

Clotting time analysis was also performed. To do so, whole human blood was collected in citrate-containing blood collection tubes. Sterile samples were placed in the wells of 24-well multi plates for the test. In brief, 100 µl of citrated blood were placed on the surfaces of the different samples (culture-treated plastic has been used as a control). After that, 20 µl of calcium chloride ($CaCl_2$) was added to the blood in order to activate the coagulation cascade ($CaCl_2$ inactivates the citrate). Samples were then incubated at 37 °C for the selected time points (0, 15, 30, 45 and 60 minutes). At each time point, 2 ml of deionized water were added to each sample to lysate the erythrocytes not entrapped in a blood clot. The aqueous solutions containing the free haemoglobin were then transferred to 96-well plates. Absorbance at a wavelength of 540 nm was recorded using a Spectra Max i3x (Molecular Devices). Absorbance is proportional to the amount of free haemoglobin. Therefore, the higher the absorbance, the higher the amount of haemoglobin, the higher the hemocompatibility.

2.8 Biological testing – antibacterial test

S. aureus (ATCC 6538) and *E. coli* (ATCC 8739) bacteria were seeded on fresh sterile Mueller–Hinton agar on Petri dishes and incubated overnight at 37 °C in an inverted position. Then, a single colony was picked and incubated into 10 ml of fresh sterile Mueller–Hinton broth overnight at 37 °C under shaking at 150 rpm. After the bacteria growth, sterile glycerol at 15% v/v was added for cryoprotection and the bacteria suspension aliquots were frozen at −20 °C. The CFU ml^{-1} of the stocks after thawing were determined by the log dilution method. In the same way, the bacteria were prepared before assay inoculation.

Kirby-Bauer susceptibility test was used in this study. Briefly, *S. aureus* and *E. coli* bacteria to be tested were taken from freeze stocks and thaw to room temperature. 100 µl containing approximately 1×0^{10} CFU ml^{-1} were spread with a Drigalski spatula into 9 cm Petri dishes coated with fresh sterile Mueller–Hinton agar. Samples were left under UV light for 15 minutes each side to sterilize before use. Afterwards, it was placed on the Petri dishes containing the bacteria and incubated overnight at 37 °C in an inverted position.

To evaluate the antibacterial activity of the released Cu from disc alloy over time in days, samples were inserted in sterile cell culture plates, added 5 ml of sterile Mueller–Hinton broth and incubated under stirring at 150 rpm and 37 °C. At different time points, *i.e.*, 6 hours, 1 day, 3 days, and 7 days, aliquots of 200 µl were taken and kept at −20 °C before use. *S. aureus* bacterial and *E. coli* stock suspension were thawed and diluted to a final concentration of 1×10^6 CFU ml^{-1} (OD_{600} *ca.* 0.020) in sterile Mueller–Hinton broth in a 96-well culture plate. Subsequently, 100 µl of aliquots were mixed with 100 µl of bacteria inoculum. Stainless steel was used as negative control and the antibiotic Trimethoprim as positive control (25 µg ml^{-1}). Plates were incubated at 37 °C under shaking at 150 rpm until OD_{600} reached 0.6–0.8. The OD_{600} of the samples were determined and compared to the negative controls. Then, the bacterial survival was calculated using the following equation. Experiments were conducted in triplicates.

$$\text{Bacterial survival } [\%] = \frac{\text{Sample } OD_{600}}{\text{Blank } OD_{600}} \times 100 \qquad (4)$$

3. Results and discussion

3.1 Microstructure and mechanical properties

The first milestone of the present work was to investigate a proper heat treatment to obtain good overall conditions for the

intended biomedical application. Selection criteria were based on the following considerations:

• Obtaining a non-ferromagnetic macroscopic behavior by limiting the amount of ferromagnetic ferritic phases.

• Achieving an adequate mechanical performance. A microstructure, consisting of small grains and precipitates that reinforce the matrix to obtain higher strength than Fe and FeMn alloys, maintaining an elongation to failure above 25%, was targeted.

• Aiming at conditions that are expected to lead to favorable degradation performance in human body environment by means of a fine and homogenous microstructure.

XRD measurements were performed on the heat-treated samples to determine the crystallographic phases. Results are shown in Fig. 2.

The microstructure of the alloy consisted of two main phases – FCC γ-austenite and HCP ε-martensite – after all heat treatments. In addition, depending on the temperature and cooling conditions, a variable quantity of α-martensite was present, best observed by two distinct peaks at 44.9° and 65.0°. The water-quenched samples showed significantly higher α-martensite content than the slowly furnace-cooled ones.

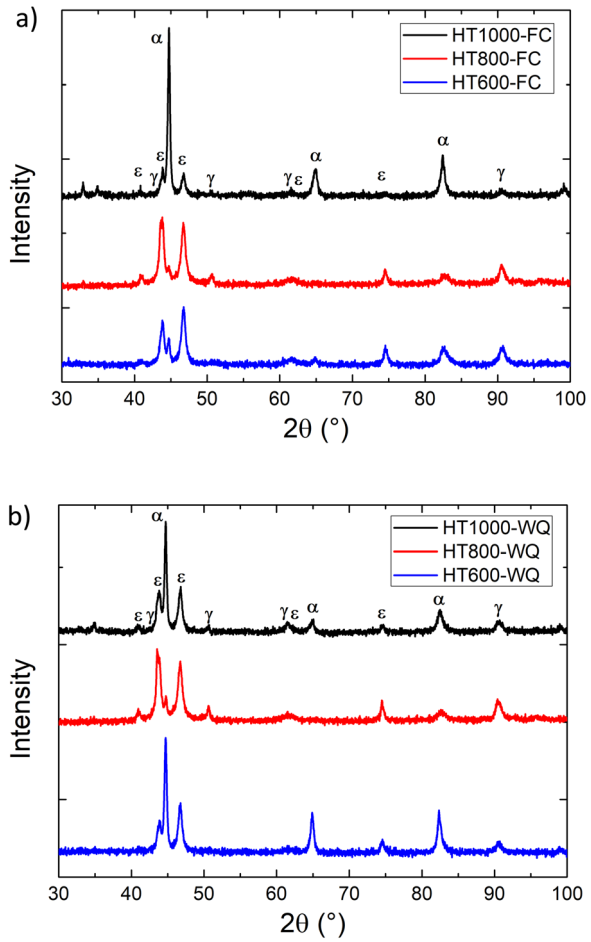

Fig. 2 XRD spectra of Fe–Mn–Si–Cu after cold rolling and heat treatment at various temperatures followed by (a) furnace cooling; (b) water quenching.

Table 3 Phase fractions of samples after various heat treatments calculated with Rietveld-method

	HT600		HT800		HT1000	
Phase	FC	WQ	FC	WQ	FC	WQ
FCC [%]	19.5	79	30	29.3	0	0.1
BCC [%]	52.4	72.7	4.4	5.9	29	56.1
HCP [%]	28.1	19.4	65.6	64.8	71	43.8
Rexp	1.75	1.8	1.88	1.86	1.77	1.8

In the samples that were heat treated at 600 °C or 800 °C for 1 h followed by furnace cooling, the amount of α-martensite was reduced to a minimum, while it was increased after heat treatment at 1000 °C for 1 h. The different phase fractions calculated by using Rietveld-method are presented in Table 3.

The presence of α-martensite at the grain boundaries, where the alloy chemistry could vary slightly from the bulk, was also reported by Stanford *et al.* after annealing of a Fe–Mn–Si-based shape-memory alloy at 1000 °C for 1 hour.[33] It seems that α-martensite formed at higher temperatures and transform into γ-austenite upon cooling, while in the water quenched samples a higher amount of α-phase remains frozen in the microstructure. The presence of α-phase is controversially discussed, as it increases the magnetic susceptibility, thus inhibiting the use of medical imaging techniques like magnetic resonance spectroscopy. On the other hand, small quantities of α-martensite could have a negligible impact on the magnetic behavior,[34] and an α + ε containing microstructure could improve the degradation rate of Fe–Mn alloys.[35] Concerning the mechanical properties, a microstructure containing both γ- and ε-phases is desired, as it indicates a low stacking fault energy, which in turn is related to an optimal strain hardening behavior due to twinning induced plasticity (TWIP) and transformation induced plasticity (TRIP) effects.[36]

In this light, the mechanical properties of as-cold-rolled sample and after heat treatments at 600 °C and 800 °C for 1 h followed by furnace cooling were investigated. Test curves and a summary of results are presented in Fig. 3 and in Table 4, respectively.

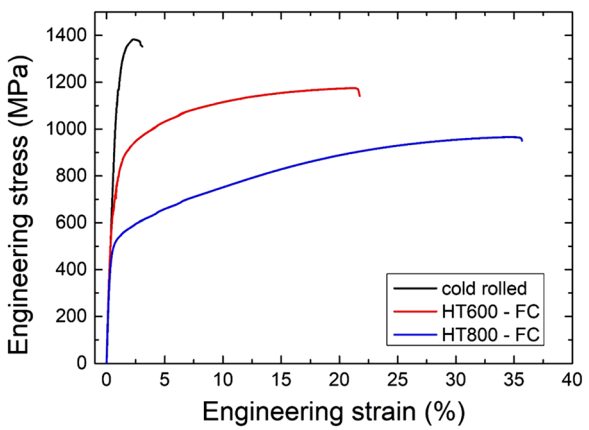

Fig. 3 Representative tensile curves of Fe–Mn–Si–Cu annealed at different temperatures.

Table 4 Summary of tensile test results of Fe–Mn–Si–Cu alloy after rolling and heat treatments, where E = Young's modulus, YS = yield strength, UTS = ultimate tensile strength, E_f = elongation to failure

Condition	E [GPa]	YS [MPa]	UTS [MPa]	E_f [%]
Cold rolled (CW = 25%)	156.9 ± 6.3	1104 ± 124	1383 ± 200	2.9 ± 0.7
HT600-FC	144.6 ± 9.4	691 ± 71	1176 ± 140	17.7 ± 1.3
HT800-FC	149.6 ± 2.8	481 ± 86	966 ± 85	37.5 ± 4.6

The alloy exhibits promising mechanical properties: the Young's Modulus is significantly lower than the one of Fe (in the range of 204–212 GPa) or medical steel 316L (193 GPa[37]), suggesting that the present alloy may facilitate the design orthopedic implants, which are less prone to induce stress shielding effects compared to common Fe-based medical materials. Furthermore, the combination of high yield stress, elevated ultimate tensile stress and with relative long elongations to failure permits a good performance against rupture both in cardiovascular and orthopedic applications. In cold-rolled condition, the material was stronger and more brittle, showing rupture below 3% elongation at elevated stresses. After annealing at 600 °C, the material became much more ductile and yield strength was decreased. At higher temperature (800 °C for 1 h), the material gained even more ductility at the expense of the mechanical resistance. These results showed that the material offers interesting opportunities to be customized to the requirements of various medical implants, exceeding the properties of 316L steel (cast: UTS = 517 MPa; YS = 172 MPa; E_f = 23%; wrought: UTS = 580 MPa; YS = 290 MPa; E_f = 42%[37]).

The HT800-FC condition was selected for more in-depth characterization, as it showed an interesting combination of good mechanical properties and low amount of α-martensite. Optical Microscopy analysis was performed to evaluate the morphology of the microstructure in homogenized ingot, cold rolled and final annealed conditions (Fig. 4).

The microstructure of the homogenized ingot was characterized by coarse austenitic grains (grain size >500 μm), in which the twinned martensitic structure could be observed (Fig. 4(a)). Furthermore, two types of particles, Mn (S, Se) inclusions and Cu-rich B2 second phases, were randomly distributed both inside the grains and at their boundaries. S and Se are typical impurities present in the raw materials. No peaks could be associated to Cu-rich B2 particles with FCC structure in XRD experiment, as their quantity was presumably below the detection limit. In addition, their signal would partially overlap with the major γ-austenite reflections.

After rolling, the microstructure became distorted (Fig. 4(b)). In the rolled and annealed conditions, a finer microstructure, with an average grain size in the range of 1.84 ± 0.11 μm could be observed (Fig. 4(c)). In addition, the secondary phases were refined by the rolling actions, becoming smaller despite the heat input from the final annealing (Fig. 4(d)). A study on the dissolution and precipitation behavior of the B2 Cu particles was conducted by heat treatments and SEM analysis (Fig. 5).

The micrographs demonstrated the impact of heat treatment on the Cu-rich phase. After lower temperature annealing, *i.e.* 1 h at 600 °C and 800 °C, the particles had a size of a few μm and had a polygonal shape. At 800 °C for 1 h, they started to grow slightly, but their growth was likely limited by the low Cu content in the alloy. After heat treatment at 900 °C for 1 h, the phase showed changes in the morphology: particle became rounder, as they started to dissolve along the edges. However, the driving force for dissolution and diffusion was apparently too low for dissolving the particles in the matrix. Finally, at even higher temperatures (1000 °C for 1 h), the particle number was significantly reduced, and the observed particles were smaller.

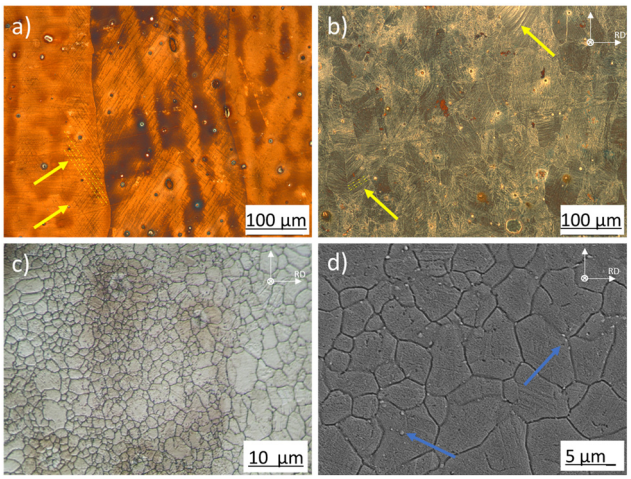

Fig. 4 Microstructure of Fe–Mn–Si–Cu alloy: optical micrographs of (a) homogenized Ingot (50×); (b) cold rolled sheet (50×); (c) final annealed sheet (800 °C for 1 h, prepared with furnace cooling, 500×); (d) close-up SEM micrograph of final annealed sheet (1000×), examples for ε-martensite are indicated by yellow arrows and dashed lines; Cu-rich phase particles are marked by blue arrows. SEM was used for revealing the finest features in HT1000 not visible in OM. The white inlet indicats the rolling direction.

By the above presented incremental screening and selection, it was possible to identify a processing condition suitable for the present study. As previously stated, the ideal alloy would display suitable mechanical properties, fine grain size with a metallic matrix based on γ-austenite and ε-martensite, and a homogeneous distribution of small Cu-rich phases able to act as noble sites, accelerating degradation in physiological environment by galvanic coupling. Based on these considerations, 800 °C for 1 h heat treatment was selected as preferred condition for the preparation of samples for degradation analysis and biological tests.

3.2 Degradation testing

Potentiodynamic tests, were conducted on Fe–Mn–Si–Cu samples for the homogenized alloy and for the cold rolled and

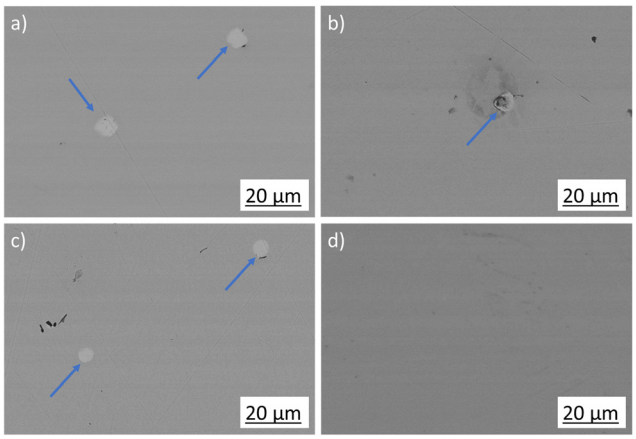

Fig. 5 Dissolution and precipitation behavior of B2 Cu particles in the heat-treated samples: (a) 600 °C for 1 h; (b) 800 °C for 1 h; (c) 900 °C for 1 h; (d) 1000 °C for 1 h. Blue arrows indicate Cu-rich particles.

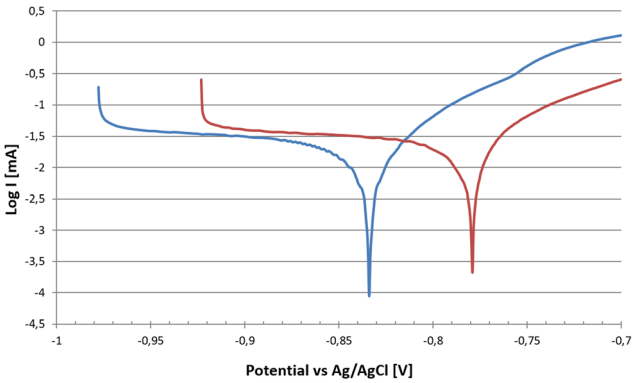

Fig. 6 Tafel curves of Fe–Mn–Si–Cu in homogenized ingot and cold rolled conditions at the end of the 3.5 h corrosion test protocol.

annealed at 800 °C for 1 h condition. This set-up allowed for the evaluation of alloy degradation prior to formation of a significant passivation layer, *i.e.* whenever the metallic surface itself is exposed to PBS media. Tafel Plot curves are shown in Fig. 6, while corrosion results are presented in Table 5.

After rolling and final annealing, the open circuit potential became less negative, *i.e.* the material was less prone to corrosion, presumably due to the homogenizing effect on local chemical composition by rolling and heat treatment operations. A decrease of the open circuit electrochemical potential by reducing grain size was also observed in other studies on pure Fe.[38,39] On the other hand, as visible in Table 5, the corrosion rate was higher within the first 3.5 hours due to the microstructure, consisting of smaller grains and a higher number of dislocations arising from plastic deformation and only partially annihilated after annealing.[40] Compared to the ternary Fe–30Mn–5Si prepared with the same processing route,[32] which presented a degradation rate of 0.18 ± 0.04 mm per y, the corrosion was accelerated, despite registering a less negative potential and a higher resistance in corrosimetry after 3.5 h of testing.

Furthermore, the distribution of small-sized Cu-rich particles inducing electrogalvanic corrosion, as demonstrated by SEM-EDX analysis in Fig. 7, was expected to increase the corrosion rate.[41] As they can be expected to be nobler than the surrounding matrix, the latter was preferentially corroded as evidenced by the distribution of O-rich areas in the color maps of Fig. 7(b) and (c). At the end of the test, the resistance of rolled and annealed samples was higher than the ingot samples, therefore slowing the degradation of the alloy. This suggests that the material showed a stronger passivation tendency, favored by the fine-grained microstructure.[42] This observation was also supported by static immersion degradation tests, whose results are presented in Table 6 in terms of weight loss.

The degradation rate during static immersion tests was much higher for Fe–Mn–Si than for Fe–Mn–Si–Cu alloy, giving rise to an opposite trend with respect to the one observed by potential-dynamic testing within the 3.5 hours. This trend inversion may be ascribed to the faster passivation of Fe–Mn–Si–Cu alloy related to the presence of fine Cu-rich particles (*cf.* Fig. 7(a)) and to the finer grain size (1.85 µm in Fe–Mn–Si–Cu *vs.* 35 µm in Fe–Mn–Si[32]). The higher corrosion rate that is measured in potential-dynamic tests and the presence of several small noble sites is expected to lead to a fast and homogenous passivation that progresses significantly during the initial stages of corrosion,[32] as observed by Gollapudi *et al.*[42] in a study on biodegradable Mg, too. Therefore, the microstructure of Fe–Mn–Si–Cu was more prone to develop passivation, leading to a lower mass loss and average degradation rate in the long term, compared to the Fe–Mn–Si alloy. The combination of low degradation rate and high strength could make the Fe–Mn–Si–Cu alloy particularly suitable for thin devices, which require a high functionality for a period lasting from several months to a couple of years. In addition, the slow dissolution and therefore minor daily release of Mn and Cu ions could be beneficial regarding biocompatibility concerns. Considering the low corrosion rates, the daily body uptake of such minority elements will be small.

Table 5 Pseudo-dynamic corrosion test results from potentiostat measurements at the end of the 3.5 h protocol, where Ω is electrical resistance measured in corrosimetry, E_{Oc} is the open circuit potential from Tafel plot and C.R. is the calculated corrosion rate according to eqn (2)

Alloy/condition	Ω [Ohm]	E_{Oc} [V]	C.R. [mm per y]
FeMnSi Ingot[a32]	352 ± 60	− 0.86 ± 0.01	0.18 ± 0.04
FeMnSiCu Ingot (Homogenized)	544 ± 29	− 0.83 ± 0.01	0.30 ± 0.03
FeMnSiCu rolled (HT800-FC)	602 ± 38	− 0.80 ± 0.02	0.32 ± 0.07

[a] Ref. 32 reports result on a ternary Fe–30Mn–5Si prepared with the same processing route.

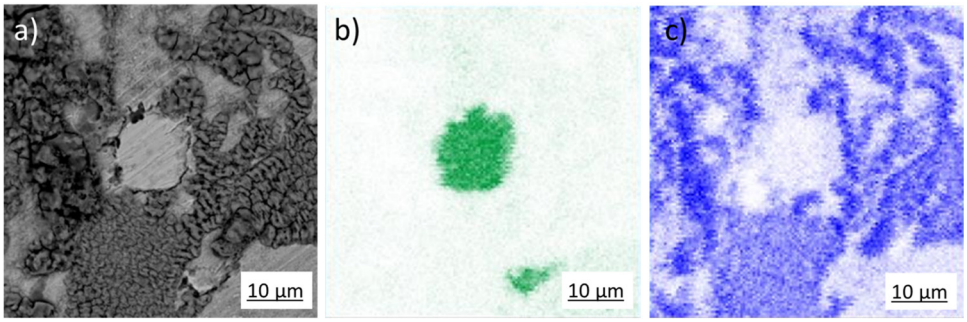

Fig. 7 Electro-galvanic corrosion in the vicinity of Cu-particles as observed by SEM: (a) corroded microstructure after 3.5 h pseudo-dynamic corrosion testing; (b) EDX color map highlighting copper; (c) EDX color map highlighting oxygen.

Table 6 Static immersion degradation results after testing for 14 days in modified Hanks's solution

Sample	w_{loss} [g]	D.R. [mm per y]
FeMnSi rolled[a32]	0.054 ± 0.023	0.450 ± 0.190
FeMnSiCu rolled (HT800-FC)	0.020 ± 0.001	0.167 ± 0.008

[a] Ref. 32 reports result on a ternary Fe–30Mn–5Si prepared with the same processing route.

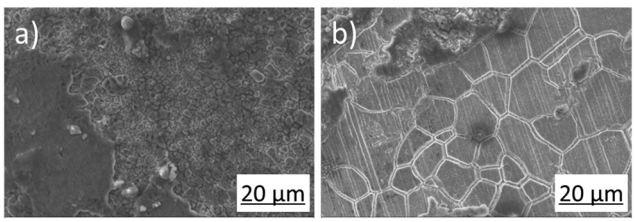

Fig. 8 Micrographs of corroded sample surface after static immersion test for 14 days: (a) area with passivated surface by corrosion scale; (b) surface area in which corrosion products detached by cleaning.

The Fe–Mn–Si–Cu sample surface, after static immersion test and subsequent cleaning, is shown in Fig. 8.

Before cleaning, the whole sample was covered by a homogenous and continuous corrosion scale like the one visible in Fig. 8(a), which was then partially detached, so that the bare metal surface could be observed (Fig. 8(b)). The scale was found to chiefly consist of Fe and Mn carbonates, but traces of all alloying elements, as well as of the elements composing the modified Hank solution, were revealed by EDX, too, it may be observed that, in the areas where the corrosion products were detached, corrosion proceeded primarily along the grain boundaries, which were noted to be enriched in Cu with respect to the matrix. It was also evident that the corrosion layer was less stable in zones with bigger grains. Comparing Fig. 8(b) with the microstructure shown in Fig. 4(c), it is evident that the average grain size in zones that are not covered by corrosion layer after cleaning was significantly higher than the one of the cold-rolled and annealed sample.

3.3 Cytotoxicity indirect assay

In the cytotoxicity indirect assays, different cell types were treated with different dilutions (100, 10 and 1%) of extracts obtained from SS 316L stainless steel (SS316L), and Fe–Mn–Si–Cu alloy (FeMnSiCu). Standard culture medium was used as a control (CTRL). Cell viability was measured after 1 day of incubation by means of a resazurin salt solution assay.

The prepared eluates containing the degradation products used for the cytotoxicity assays own a heterogeneous composition. In fact, carbonates, phosphates, oxides hydroxides, oxyhydroxides of the metallic components with a low solubility as well as metallic ions, leaking from the exposed alloy are present. The longer the specimens were exposed to the medium, the higher is the amount of total released degradation products coming from the substrate: this means that, after an exposure period of 7 days, the ionic and degradation product content of the extracts has a higher concentration than the one generated from a shorter exposure to the medium, (1 or 3 days). For the corrosion mechanism it is usually and schematically assumed that (1) the ions/degradation products are always the same during the degradation process, and (2) they are produced constantly (with a constant rate) during the aforementioned process, so that it is possible to suppose that, for the chosen duration, the ion concentration of the extracts is roughly proportional to the exposure time. It is assumed that the diluted extracts, with concentrations of 100%, 10% and 1%, after material exposition of 1, 3 and 7 days (9 different conditions), contained more or less the same chemical species. However, the relative ratio of metal ion/degradation product varies for the different concentrations, because of the different exposure times and dilution levels.

The results of the indirect cytotoxicity assays performed on HDFs are presented in Fig. 9, showing the mean fluorescence ± SD recorded from HDFs treated with the different experimental conditions. Results have been normalized against the CTRL condition.

As it can be noted, the 100% dilution (meaning the undiluted extracts obtained from the samples) shows that the extracts obtained from the Fe–Mn–Si–Cu conditions significantly decreased the cell viability compared to both the CTRL and SS316L conditions ($p < 0.001$). No statistical significance was noted between the CTRL and SS316L conditions. With the 10% dilution, once again the Fe–Mn–Si–Cu alloy extracts were able to significantly decrease the treated HDFs viability compared to both the CTRL and SS316L conditions ($p < 0.001$).

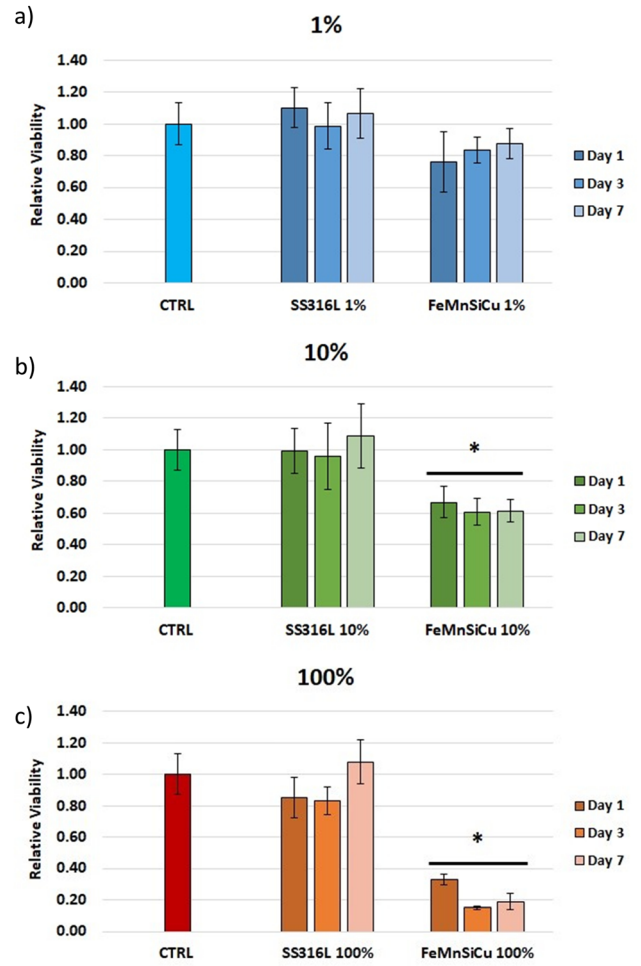

Fig. 9 Indirect cytotoxicity assay on HDFs: (a) 1% dilution; (b) 10% dilution; (c) 100% dilution. *$p < 0.001$ *vs.* CTRL, SS316L and FeMnSiCu conditions.

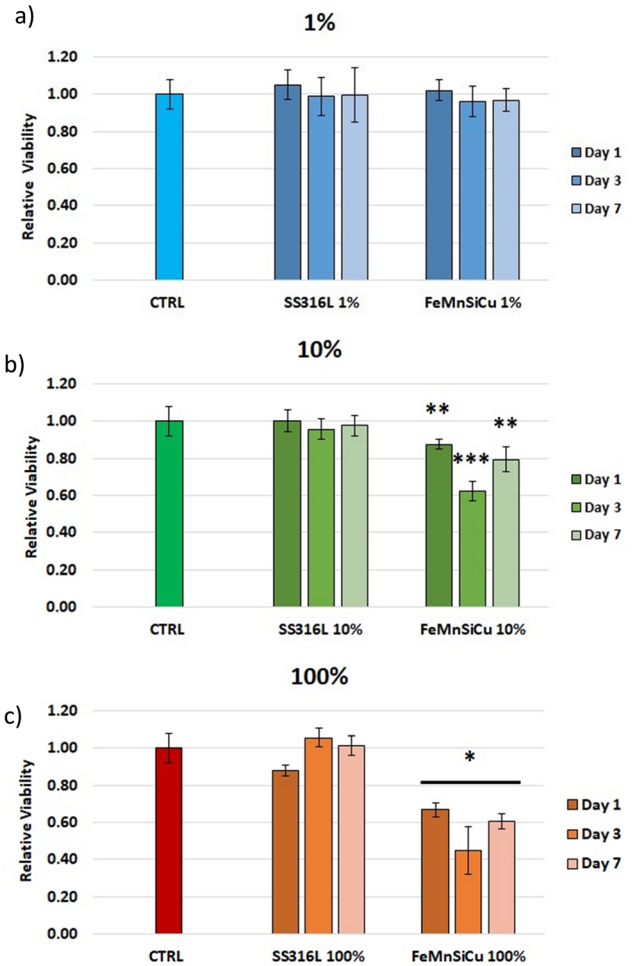

Fig. 10 Indirect cytotoxicity assay on Saos-2: (a) 1% dilution; (b) 10% dilution; (c) 100% dilution.

However, the decrease was significantly lower than the one observed with the 100% dilution ($p < 0.001$). No statistical differences were noted between the CTRL and SS316L conditions. Finally, with the 1% dilution, no significant differences were noted among all the tested conditions.

Regarding Saos-2 cells (Fig. 10), at the 100% dilution the extracts obtained from the Fe–Mn–Si–Cu samples significantly decreased the viability of the treated cells compared to both the CTRL and SS316L conditions ($p < 0.001$). No differences were noted between the CTRL and SS316L conditions. With the 10% dilution, the Fe–Mn–Si–Cu extracts significantly decreased the viability of the treated Saos-2 cell against both the other experimental conditions ($p < 0.01$ at day 1 and 7, $p < 0.001$ *vs.* day 3). As previously noted with HDFs, the 10%-related viability decrease was lower than the one obtained with the 100% dilution ($p < 0.001$). The 1% dilution did not induce any significant change in the viability of the treated cells with all the condition tested.

Concerning the indirect viability test performed on HUVECs (Fig. 11), the Fe–Mn–Si–Cu sample induced a significant decrease in cell viability with all the tested dilution compared to both the CTRL and SS316L conditions ($p < 0.001$). Interestingly, as previously reported with both HDFs and Saos-2 cells, the higher was the dilution, the higher was the viability of the treated HUVECs. In fact, the viability recorded for the 1% dilution was significantly higher than the ones recorded at both 10% and 100% dilutions ($p < 0.001$). No significant differences were noted between the 10% and 100% dilutions.

Finally, concerning the HUASMCs results (Fig. 12), with the 100% dilution, the extracts obtained from Fe–Mn–Si–Cu samples significantly decreased the cell viability compared to the CTRL condition ($p < 0.001$). Interestingly, the extracts from the SS316L samples also significantly decreased the viability of the treated HUASMCs compared to the CTRL condition ($p < 0.05$). With the 10% dilution, once again the extracts from Fe–Mn–Si–Cu samples significantly reduced cell viability compared to both the CTRL and SS316L conditions ($p < 0.001$). No significant differences were noted between the CTRL and SS316L conditions. Finally, with the 1% dilutions, once again the Fe–Mn–Si–Cu extracts significantly reduced the HUASMCs viability compared to the other tested conditions ($p < 0.01$). No significant differences were noted between the CTRL and

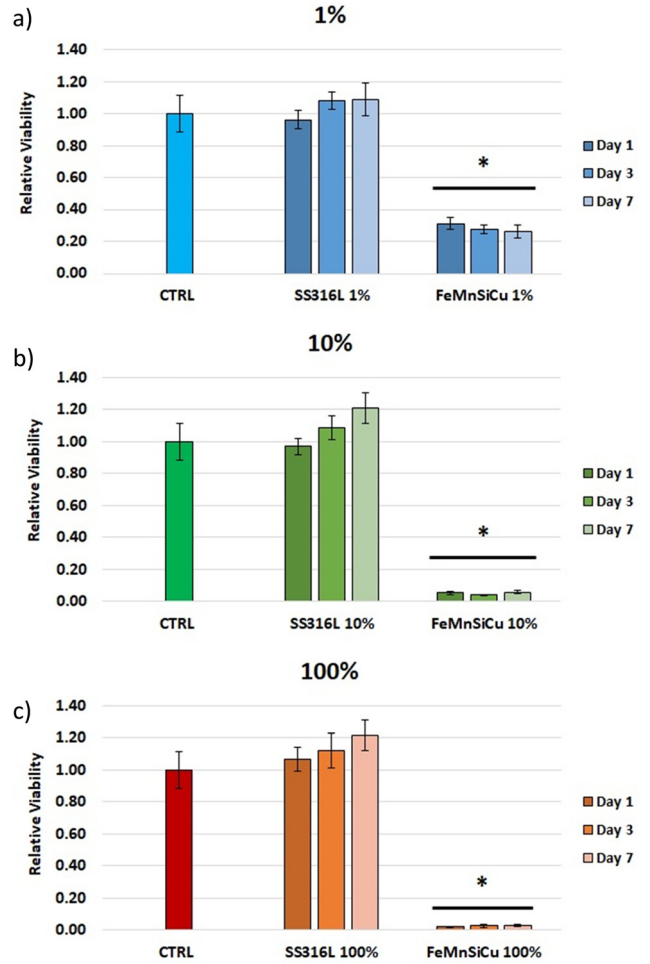

Fig. 11 Indirect cytotoxicity assay on HUVECs: (a) 1% dilution; (b) 10% dilution; (c) 100% dilution.

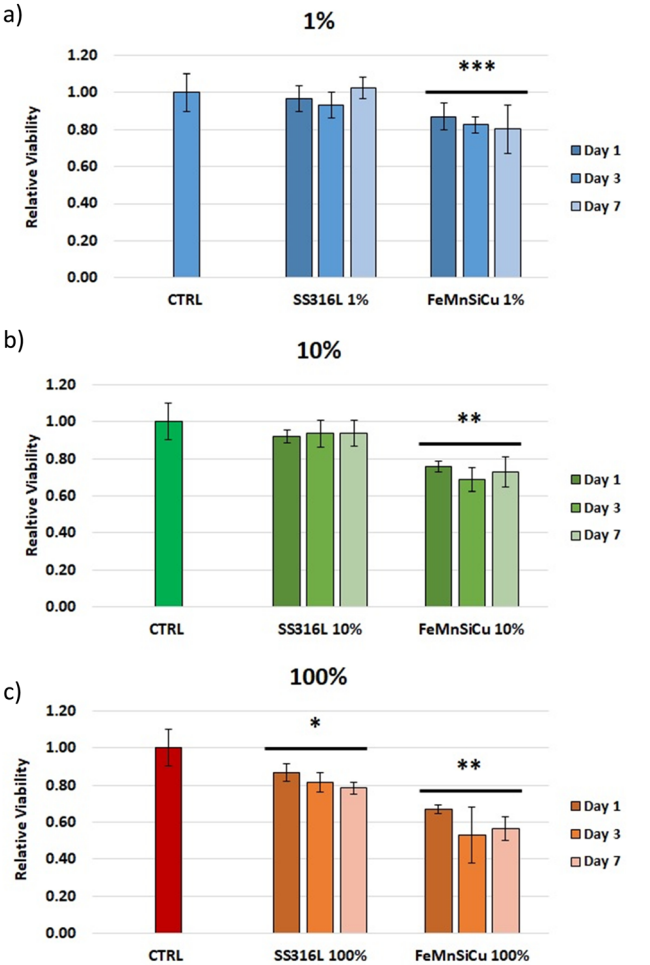

Fig. 12 Indirect cytotoxicity assay on HUASMCs: (a) 1% dilution; (b) 10% dilution; (c) 100% dilution.

SS316L conditions. Again, as previously remarked with the other tested cell lines, higher dilutions induced lower decrease in viability. The 1% dilutions induced significantly lower decreases in cell viability compared to the 100% dilution ($p < 0.01$).

It has been shown in literature on biodegradable alloys, and in particular on Fe–Mn based ones, that a dose-dependent effect exerted by the degradation products on cells viability can be observed.[43] Moreover, a previous study conducted on a Fe–Mn based alloys,[44] shows how the incubation of cells (human osteoblast) with extracts where centrifuge to remove degradation products particles, but leaving metallic ions, showed a better cell viability compared to the complete degradation products (similar to the one used in our study), showing a bigger impact of degradation product rather than metallic ions on cell cytotoxicity. Therefore, the observed cytotoxicity could mainly be attributed to the presence of degradation products particles and on the general high concentration rather than the effect of metallic ions.

The test described here can provide just a measure on the cytotoxicity of the degradation products to exclude that they do not show systematically a higher risk in biological environment. The biocompatibility of a bioabsorbable implant depends highly on the local enrichment in degradation products and will be a function of the degradation rate, its evolution over time and how they products are absorbed by the body. This last point is on the other hand affected by implant type and environmental conditions, whether they are stable or dynamic (*e.g.* exposed to body liquid flow like in a blood vessel). Results of this work are in line with observations made in previous studies, which used a similar test setup to assess the cytocompatibility of Fe–21Mn–0.7C and Fe–21Mn–0.7C–1Pd, showing that adding eluates over 2% to the cultures decrease cell viability.[45]

The rather slow degradation rates of Fe–Mn–Si–Cu could favor a low cytotoxicity in application and in adynamic environment, the concentration of degradation products could be much lower than most of the diluted eluates used in this study. However, a final conclusion on the biocompatibility of the here tested alloy can only be done by testing the material in *in vivo* models.

3.4 Hemocompatibility

The results of the performed hemolysis test (Fig. 13) show that the developed Fe–Mn–Si–Cu alloy does not induce hemolysis.

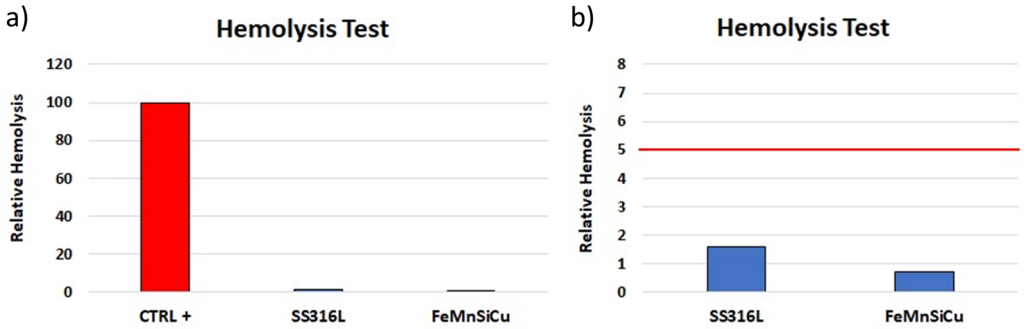

Fig. 13 (a) Results of the hemolysis test performed on SAE 316L grade stainless steel (SS-316L) and Fe–Mn–Si–Cu alloy (FeMnSiCu) compared to the positive control (CTRL+) condition; (b) differences between the tested alloys.

Fig. 14 Clotting time test performed on SAE 316L grade stainless steel (SS316L), Fe–Mn–Si–Cu (FeMnSiCu) compared to the control condition (CTRL Plast). *$p < 0.01$ *vs.* CTRL Plast 15′ and $p < 0.001$ *vs.* FeMnSiCu 15′; **$p < 0.01$ *vs.* CTRL Plast 15′; $^{\#}p < 0.001$ *vs.* CTRL Plast and SS316L 30′; $^{\S}p < 0.001$ *vs.* CTRL Plast and SS316L 45′.

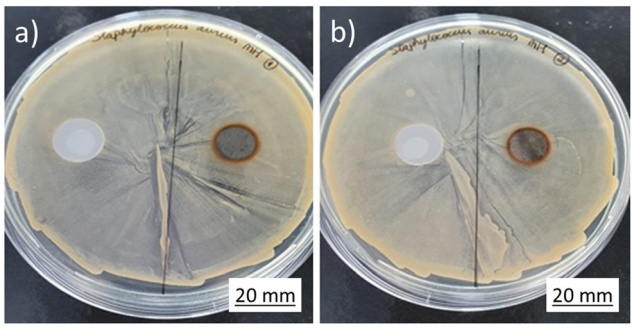

Fig. 15 Disc diffusion test. Kirby-Bauer diffusion disks incubated with *S. aureus*. Images (a) and (b) show the replicates of the performed test. No halo of inhibition was seen around the Fe–Mn–Si–Cu samples.

In fact, for a material to be considered hemolytic, it must induce hemolysis at percentages higher than 5%, hence the tested alloy is not hemolytic.

Regarding the clotting time test results (Fig. 14), at the time point of 0 minutes, as expected, the blood did not coagulate. Moreover, no differences were noted among the different conditions. This value has been kept as the reference for the test (100% = maximal hemocompatibility). After 15 minutes of incubation, the SS316L hemocompatibility was significantly reduced compared to both the CTRL ($p < 0.01$) and Fe–Mn–Si–Cu ($p < 0.001$) conditions. Moreover, the hemocompatibility of the Fe–Mn–Si–Cu was significantly higher compared to the CTRL condition ($p < 0.05$). After 30 minutes, the amount of free hemoglobin detected for the Fe–Mn–Si–Cu condition was significantly higher compared to the both the CTRL and SS316L conditions ($p < 0.001$). Again, at the 45 minutes time point, the Fe–Mn–Si–Cu condition showed an increased hemocompatibility compared to the other condition tested ($p < 0.001$). Finally, after 60 minutes of incubation, no differences were noted in between the different condition tested.

3.5 Antibacterial activity

The Kirby-Bauer diffusion disk test results are shown in Fig. 15 and 16. All the tested samples exhibited corrosion under contact with the Mueller Hinton agarose gel, as can be observed by the orange-brownish halo formed on the sample. However, no clear evidence of inhibition halo was noted in the assays for *S. aureus*. On the other hand, on the *E. coli* plates, a halo was observed, apparently related to the diffusion of the degradation products from the samples.

To test whether the developed alloy presents any indirect antibacterial effects, the dynamic indirect test was performed. Stainless steel was used as negative control for comparison while the commercial antibiotic Trimethoprim was used as positive control. Results are shown in Fig. 17. The experiment was carried out at different time points (6 hours, 1, 3 and 7 days), to accumulate the material from the dissolution of the sample. For the entire period of monitoring, SS316L and Fe–Mn–Si–Cu samples did not show any significant differences on bacteria survival, therefore indicating that the developed alloys did not present antibacterial effects towards the tested bacteria. This observation seems in contradiction with recent studies on iron-based Cu-containing alloys.[46] However, it may be worth highlighting the differences of the present study to those on other bioabsorbable Cu-containing alloys. First at all, the here prepared alloys have a rather low Cu-content compared to the 3.5 wt% of the bioabsorbable Fe–Mn–C–Cu alloy in ref. 29 that showed enhanced antibacterial properties. In addition, the Fe–Mn–C–Cu system shows a stronger tendency to grain boundary segregation,[28] which is supposed to accelerate

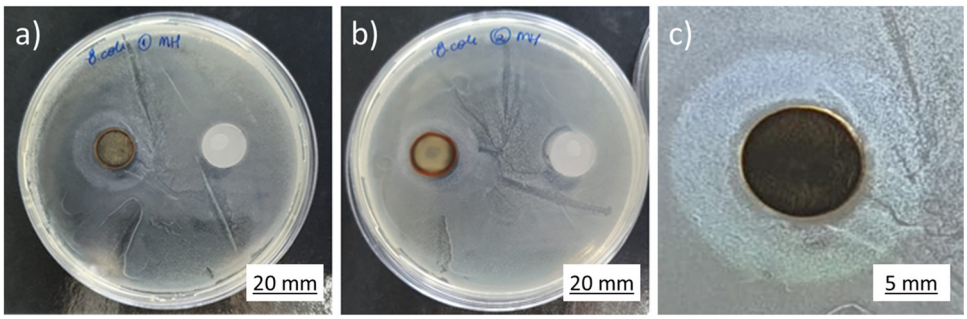

Fig. 16 Disc diffusion test. Kirby-Bauer diffusion disks incubated with *E. coli*. Images (a) and (b) show the replicates of the performed test; (c) closeup view of image A with different light to evidence the halo seen around the sample.

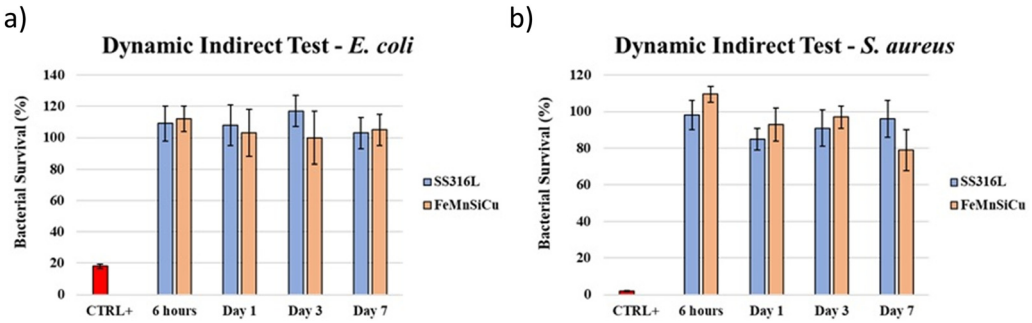

Fig. 17 The figure shows the results for the performed dynamic assays. Data are presented as bacterial survival percentage (%) ± standard deviation. 5 μg ml^{-1} Trimetroprim was used as positive control: (a) *Escherichia coli*; (b) *Staphylococcus aureus*.

corrosion and the local release of ions. Another study reports on a low Cu-containing alloy with antibacterial effect in urine system model that inhibited the formation of bacterial biofilms.[27] It is important to notice that the biological conditions are only partially comparable to the here used model of simulated body fluid. In particular, the higher reported corrosion rate in their experiment should translate also in a higher Cu-ion release. In the end, it can be expected that a threshold number of free Cu-ions is necessary to induce observable antibacterial characteristics. Indeed, Tang *et al.*, who studied the Zn_xCu_{100-x} system, that should degrade faster than Fe-based alloys and therefore release a higher number of Cu ions in an equal time interval, report that the amount of Cu needs to exceed 2 wt% for obtaining measurable antibacterial effects.[47] Presumably, the 2 wt% Cu in the current alloy and model is below the threshold of measuring antibacterial properties.

4. Summary and conclusions

A Fe–Mn–Si–Cu alloy for bioabsorbable implant applications was characterized in terms of microstructure and mechanical behavior after various heat treatments: 800 °C for 1 h treatment was selected to evaluate the alloy by its degradation behavior and performance in biological tests. The following conclusions could be drawn:

• After the optimized heat treatment at 800 °C for 1 h, followed by slow cooling, the here studied Fe–Mn–Si–Cu alloy presented a very fine grain structure and was nearly biphasic with a microstructure composed of γ-austenite, ε-martensite, Cu-rich B2 particles and some Mn(S, Se) inclusions of few microns.

• The addition of Cu resulted in a promising combination of elongation to failure and ultimate stress owing to a pronounced strain hardening behaviour.

• Degradation rates depended significantly on test conditions. In short-term potential-dynamic polarization test, Fe–Mn–Si–Cu degraded faster than the reference Fe–Mn–Si alloy. On the contrary, for 14-days static immersion test, the degradation rate was lower, namely 0.167 mm per y *vs.* 0.450 mm per y. This may be ascribed to the fact that the higher corrosion rate characterizing Fe–Mn–Si–Cu in the initial stages of degradation produced a passive layer, which reduced the degradation rate in the long term. It may be expected that, if the formation of a homogeneous protecting layer of corrosion products could be avoided, the Fe–Mn–Si–Cu alloy would degrade at a much faster rate.

• Cell tests concerning orthopaedic and cardiovascular environment showed that the degradation products obtained from the Fe–Mn–Si–Cu alloy exhibit no relevant cytotoxic effect. Decreases in cell viability noted at lower dilutions (higher concentration of degradation product) were ascribed to the high content of degradation products. Also, the test on human bone osteosarcoma cells confirmed that the degradation products are not intrinsically cytotoxic.

• The developed alloy did not present any hemotoxic effects. Interestingly, the formation of blood clot on the Fe–Mn–Si–Cu samples was delayed in comparison to both the plastic control and the reference stainless steel.

• In antibacterial tests against both Gram-positive (*S. aureus*) and Gram-negative (*E. coli*) bacteria, the antibacterial effect was less pronounced than expected. The amount of Cu introduced in the here designed Fe–Mn–Si–Cu alloy was likely below the threshold for inducing an appreciable antibacterial effect.

The present results indicate that Fe–Mn–Si–Cu could be a promising material for bioabsorbable implant application thanks to a suitable combination of mechanical performance, accelerated degradation rate in active corrosion conditions and, above all, promising biological *in vitro* test results. More research on its antibacterial properties, also considering the material preparation and test conditions, should be performed to better understand the full antibacterial potential of Cu.

Data availability

Data for this article, including X-ray spectroscopy, microscopy, mechanical testing, corrosion testing and biological testing are available at Zenodo at **https://doi.org/10.5281/zenodo.14672893**.

Conflicts of interest

The authors declare that they have no known competing financial interests or personal relationships that could have appeared to influence the work reported in this paper.

Acknowledgements

The authors would like to acknowledge Marco Pini, Giordano Carcano and Enrico Bassani from CNR ICMATE, Alessandro Gallitognotta from SAES Getters S.p.A. for their technical support in the experiments. The research project was funded by SAES Getters S.p.A., biological testing was partially funded by the Natural Science and Engineering Research Council of Canada (Collaborative Research Project), and the Government of Quebec (Ministry of Economy and Innovation under PRIMA project).

References

1 Y. Liu, Y. Zheng, X.-H. Chen, J.-A. Yang, H. Pan, D. Chen, L. Wang, J. Zhang, D. Zhu, S. Wu, K. W. K. Yeung, R.-C. Zeng, Y. Han and S. Guan, Fundamental Theory of Biodegradable Metals—Definition, Criteria, and Design, *Adv. Funct. Mater.*, 2019, **29**, 1805402.
2 X. Peng, W. Qu, Y. Jia, Y. Wang, B. Yu and J. Tian, Bioresorbable Scaffolds: Contemporary Status and Future Directions, *Front. Cardiovasc. Med.*, 2020, **7**, 1–14.
3 G. Chandra and A. Pandey, Biodegradable bone implants in orthopedic applications: a review, *Biocybern. Biomed. Eng.*, 2020, **40**, 596–610.
4 Y. F. Zheng, X. N. Gu and F. Witte, Biodegradable metals, *Mater. Sci. Eng., R*, 2014, **77**, 1–34.
5 R. Gorejova, L. Haverova, R. Orinakova, A. Orinak and M. Orinak, Recent advancements in Fe-based biodegradable materials for bone repair, *J. Mater. Sci.*, 2019, **54**, 1913–1947.
6 A. Purnama, H. Hermawan, J. Couet and D. Mantovani, Assessing the biocompatibility of degradable metallic materials: State-of-the-art and focus on the potential of genetic regulation, *Acta Biomater.*, 2010, **6**, 1800–1807.
7 G. Gasior, J. Szczepanski and A. Radtke, Biodegradable Iron-Based Materials—What Was Done and What More Can Be Done?, *Materials*, 2021, **14**, 3381.
8 M. Salama, M. F. Vaz, R. Colaço, C. Santos and M. Carmezim, Biodegradable Iron and Porous Iron: Mechanical Properties, Degradation Behaviour, Manufacturing Routes and Biomedical Applications, *J. Funct. Biomater.*, 2022, **13**, 1–31.
9 B. Wegener, A. Sichler, S. Milz, C. Sprecher, K. Pieper, W. Hermanns, V. Jansson, B. Nies, B. Kieback, P. E. Müller, V. Wegener and P. Quadbeck, Development of a novel biodegradable porous iron-based implant for bone replacement, *Sci. Rep.*, 2020, **10**, 9141.
10 Y. Qi, X. Li, Y. He, D. Zhang and J. Ding, Mechanism of Acceleration of Iron Corrosion by a Polylactide Coating, *ACS Appl. Mater. Interfaces*, 2018, **11**, 202–218.
11 J. Shi, X. Miao, H. Fu, A. Jiang, Y. F. Liu, X. L. Shi, D. Zhang and Z. Wang, *In vivo* biological safety evaluation of an iron-based bioresorbable drug-eluting stent, *Biometals*, 2020, **33**, 217–228.
12 A. Francis, Y. Yang, S. Virtanen and A. R. Boccaccini, Iron and iron-based alloys for temporary cardiovascular applications, *J. Mater. Sci.: Mater. Med.*, 2015, **26**, 138.
13 H. Hermawan, H. Alamdari and D. Mantovani, Dominique Dubé, Iron–manganese: new class of metallic degradable biomaterials prepared by powder metallurgy, *Powder Metall.*, 2008, **51**, 38–45.
14 J. W. Finley, J. G. Penland, R. E. Pettit and C. D. Davis, Dietary manganese intake and type of lipid do not affect clinical or neuropsychological measures in healthy young women, *J. Nutr.*, 2003, **133**, 2849–2856.
15 Institute of Medicine. Food and Nutrition Board. Dietary Reference Intakes for Vitamin A, Vitamin K, Arsenic, Boron, Chromium, Copper, Iodine, Iron, Manganese, Molybdenum, Nickel, Silicon, Vanadium, and Zinc Washington, DC: National Academy Press, 2001.
16 M. Schinhammer, C. M. Pecnik, F. Rechberger, A. C. Hanzi, J. F. Loffler and P. J. Uggowitzer, Recrystallization behavior, microstructure evolution and mechanical properties of biodegradable Fe–Mn–C(–Pd) TWIP alloys, *Acta Mater.*, 2012, **60**, 2746–2756.
17 S. Gambaro, C. Paternoster, B. Occhionero, J. Fiocchi, C. A. Biffi, A. Tuissi and D. Mantovani, Mechanical and degradation behavior of three Fe–Mn–C alloys for potential biomedical applications, *Mater. Today Commun.*, 2021, **27**, 102250.
18 J. Fiocchi, C. A. Biffi, S. Gambaro, C. Paternoster, D. Mantovani and A. Tuissi, Effect of laser welding on the mechanical and degradation behaviour of Fe–20Mn–0.6C bioabsorbable alloy, *J. Mater. Res. Technol.*, 2020, **9**, 13474–13482.

19 B. Liu, Y. F. Zheng and L. Ruan, *In vitro* investigation of $Fe_{30}Mn_6Si$ shape memory alloy as potential biodegradable metallic material, *Mater. Lett.*, 2011, **65**, 540–543.
20 M. Fântânariu, L. C. Trinca, C. Solcan, A. Trofin, S. Strungaru, E. V. Sindilar, G. Plavan and S. Stanciu, A new Fe–Mn–Si alloplastic biomaterial as bone grafting material: *In vivo* study, *Appl. Surf. Sci.*, 2015, **352**, 129–139.
21 A. M. Roman, V. Geantă, R. Cimpoesu, C. Munteanu, N. M. Lohan, G. Zegan, E. R. Cernei, I. Ionită, N. Cimpoesu and N. Ioanid, *In vitro* Analysis of FeMn-Si Smart Biodegradable Alloy, *Materials*, 2022, **15**, 568.
22 Y. P. Feng, A. Blanquer, J. Fornell, H. Zhang, P. Solsona, M. D. Baro, S. Surinach, E. Ibanez, E. Garcıa-Lecina, X. Wei, R. Li, L. Barrios, E. Pellicer, C. Nogues and J. Sort, Novel Fe–Mn–Si–Pd alloys: insights into mechanical, magnetic, corrosion resistance and biocompatibility performances, *J. Mater. Chem. B*, 2016, **4**, 6402–6412.
23 L. C. Trincă, L. Burtan, D. Mareci, B. M. Fernández-Pérez, I. Stoleriu, T. Stanciu, S. Stanciu, C. Solcan, J. Izquierdo and R. M. Souto, Evaluation of *in vitro* corrosion resistance and *in vivo* osseointegration properties of a FeMnSiCa alloy as potential degradable implant biomaterial, *Mater. Sci. Eng., C*, 2021, **118**, 11143.
24 M. S. Dargusch, J. Venezuela, A. Dehghan-Manshadi, S. Johnston, N. Yang, K. Mardon, C. Lau and R. Allavena, *In Vivo* Evaluation of Bioabsorbable Fe–35Mn–1Ag: First Reports on *In Vivo* Hydrogen Gas Evolution in Fe-Based Implants, *Adv. Healthcare Mater.*, 2021, **10**, 2000667.
25 S. Loffredo, S. Gambaro, F. Copes, C. Paternoster, N. Giguère, M. Vedani and D. Mantovani, Effect of silver in thermal treatments of Fe–Mn–C degradable metals: Implications for stent processing, *Bioact. Mater.*, 2022, **12**, 30–41.
26 J. T. Krüger, K.-P. Hoyer, F. Hengsbach and M. Schaper, Formation of insoluble silver-phases in an iron-manganese matrix for bioresorbable implants using varying laser beam melting strategies, *J. Mater. Res. Technol.*, 2022, **19**, 2369–2387.
27 Z. Ma, M. Gao, D. Na, Y. Li, L. Tan and K. Yang, Study on a biodegradable antibacterial Fe–Mn–C–Cu alloy as urinary implant material, *Mater. Sci. Eng., C*, 2019, **103**, 109718.
28 S. Wei, Z. Ma, L. Tan, J. Chen, R. D. K. Misra and K. Yang, Effect of copper content on the biodegradation behavior of Fe–Mn–C alloy system, *Mater. Technol.*, 2022, **37**(9), 1109–1119.
29 B. Paul, A. Kiel, M. Otto, T. Gemming, V. Hoffmann, L. Giebeler, B. Kaltschmidt, A. Hütten, A. Gebert, B. Kaltschmidt, C. Kaltschmidt and J. Hufenbach, Inherent Antibacterial Properties of Biodegradable FeMnC(Cu) Alloys for Implant Application, *ACS Appl. Bio Mater.*, 2024, **7**, 839–852.
30 A. Coda, J. N. Lemke, A. Tuissi, J. Fiocchi and C. A. Biffi, *Bioresorbable Fe–Mn–Si–X Alloys For Medical Implants*, *European Patent Office*, WO/2021/204811, 2021.
31 A. Coda, J. N. Lemke, A. Tuissi and J. Fiocchi, *Bioresorbable Pseudoelastic Fe–Mn–X–Y Alloys For Medical Implants*, *European Pat. Office*, WO/2021/16533, 2021.
32 J. Fiocchi, J. N. Lemke, S. Zilio, C. A. Biffi, A. Coda and A. Tuissi, The effect of Si addition and thermomechanical processing in an Fe–Mn alloy for biodegradable implants: Mechanical performance and degradation behavior, *Mater. Today Commun.*, 2021, **27**, 102447.
33 N. Stanford, D. P. Dunne and B. J. Monaghan, Austenite stability in Fe–Mn–Si-based shape memory alloys, *J. Alloys Compd.*, 2007, **430**, 107–115.
34 U. Sarı and T. Kırındı, Effect of Mn content on the austenite–martensite phases and magnetic properties in Fe–Mn–Co alloys, *Mater. Chem. Phys.*, 2011, **130**, 738–742.
35 P. Liu, H. Wu, L. Liang, D. Song, J. Liu, X. Ma, K. Li, Q. Fang, Y. Tian and I. Baker, Microstructure, mechanical properties and corrosion behavior of additively-manufactured Fe–Mn alloys, *Mater. Sci. Eng., A*, 2022, **852**, 143585.
36 A. Dumay, J.-P. Chateau, S. Allain, S. Migot and O. Bouaziz, Dependence of tensile deformation behavior of TWIP steels on stacking fault energy, temperature and strain rate, *Acta Mater.*, 2010, **58**, 5129–5141.
37 A. Hansel, M. Mori, M. Fujishima, Y. Oda, G. Hyatt, E. Lavernia and J.-P. Delplanque, Study on consistently optimum deposition conditions of typical metal material using additive/subtractive hybrid machine tool, *Procedia CIRP*, 2016, **46**, 579–582.
38 L. Jinlong and L. Hongyun, The effects of cold rolling temperature on corrosion resistance of pure iron, *Appl. Surf. Sci.*, 2014, **317**, 125–130.
39 V. Afshari and C. Dehghanian, Effects of grain size on the electrochemical corrosion behaviour of electrodeposited nanocrystalline Fe coatings in alkaline solution, *Corros. Sci.*, 2009, **51**, 1844–1849.
40 J. L. Dossett and G. E. Totten, Introduction to Steel Heat Treatment, *Steel Heat Treating Fundamentals and Processes, ASM Handbook*, ASM International, 2013, vol. 4A, pp. 3–25.
41 M. Schinhammer, A. C. Hänzi, J. F. Löffler and P. J. Uggowitzer, Design strategy for biodegradable Fe-based alloys for medical applications, *Acta Biomater.*, 2010, **6**(5), 1705–1713.
42 S. Gollapudi, Grain size distribution effects on the corrosion behavior of materials, *Corros. Sci.*, 2012, **62**, 90–94.
43 S. A. Elborolosy, L. A. Hussein, H. Mahran, H. R. Ammar, S. Sivasankaran, S. F. A. El-Ghani, M. Y. Abdelfattah, A. W. Abou-Zeid, S. H. Ibrahim and M. M. Elshamaa, Evaluation of the biocompatibility, antibacterial and anticancer effects of a novel nano-structured Fe–Mn-based biodegradable alloys *in vitro* study, *Heliyon*, 2023, **9**(11), 20932.
44 M. Caligari Conti, D. Aquilina, C. Paternoster, D. Vella, E. Sinagra, D. Mantovani, G. Cassar, P. Schembri Wismayer and J. Buhagiar, Influence of cold rolling on *in vitro* cytotoxicity and electrochemical behaviour of an Fe–Mn–C biodegradable alloy in physiological solutions, *Heliyon*, 2018, **4**(11), e00926.
45 M. Schinhammer, I. Gerber, A. C. Hänzi and P. J. Uggowitzer, On the cytocompatibility of biodegradable Fe-based alloys, *Mater. Sci. Eng., C*, 2013, **33**(2), 782–789.

46 E. Zhang, S. Fu, R.-X. Wang, H.-X. Li, Y. Liu, Z.-Q. Ma, G.-K. Liu, C.-S. Zhu, G.-W. Qin and D.-F. Chen, Role of Cu element in biomedical metal alloy design, *Rare Met.*, 2019, **38**(6), 476–494.

47 Z. Tang, J. Niu, H. Huang, H. Zhang, J. Pei, J. Ou and G. Yuan, Potential biodegradable Zn–Cu binary alloys developed for cardiovascular implant applications, *J. Mech. Behav. Biomed. Mater.*, 2017, **72**, 182–191.

